

1 **Deriving seasonal dynamics in ecosystem properties of semi-**  
2 **arid savanna grasslands from in situ based hyperspectral**  
3 **reflectance**

4  
5 **Torbern Tagesson\***<sup>1</sup>, **Rasmus Fensholt**<sup>1</sup>, **Silvia Huber**<sup>2</sup>, **Stephanie Horion**<sup>1</sup>, **Idrissa Guiro**<sup>3</sup>,  
6 **Andrea Ehammer**<sup>1</sup>, **Jonas Ardö**<sup>4</sup>

7  
8 <sup>1</sup>Department of Geosciences and Natural Resource Management, University of Copenhagen, Øster  
9 Voldgade 10, DK-1350 Copenhagen, Denmark; E-Mails: torbern.tagesson@ign.ku.dk, rf@ign.ku.dk,  
10 stephanie.horion@ign.ku.dk, andrea.ehammer@ign.ku.dk

11  
12 <sup>2</sup>DHI GRAS A/S, Agern Allé 5, DK-2970 Hørsholm, Denmark; E-mail: shu@dhi-gras.com

13  
14 <sup>3</sup>Laboratoire d'Enseignement et de Recherche en Géomatique, Ecole Supérieure Polytechnique,  
15 Université Cheikh Anta Diop de Dakar, BP 25275 Dakar-Fann, Senegal; E-mail: idyguiro@yahoo.fr

16  
17 <sup>4</sup>Department of Physical Geography and Ecosystem Science, Lund University, Sölvegatan 12, SE-223  
18 62 Lund, Sweden, E-mail: jonas.ardo@nateko.lu.se

19  
20 \*Correspondence to: Torbern Tagesson; torbern.tagesson@ign.ku.dk, Tel. nr: +46-704 99 39 36, Fax  
21 nr: +45 35 32 25 01, Department of Geosciences and Natural Resource Management, University of  
22 Copenhagen, Øster Voldgade 10, DK-1350 Copenhagen, Denmark

23 **Abstract**

24 This paper investigates how hyperspectral reflectance (between 350 and 1800 nm) can be used to infer  
25 ecosystem properties for a semi-arid savanna grassland in West Africa using a unique in situ based  
26 multi-angular dataset of hemispherical conical reflectance factor (HCRF) measurements. Relationships  
27 between seasonal dynamics in hyperspectral HCRF, and ecosystem properties (biomass, gross primary  
28 productivity (GPP), light use efficiency (LUE), and fraction of photosynthetically active radiation  
29 absorbed by vegetation (FAPAR)) were analysed. HCRF data ( $\rho$ ) were used to study the relationship  
30 between normalised difference spectral indices (NDSI) and the measured ecosystem properties. Finally,  
31 also the effects of variable sun sensor viewing geometry on different NDSI wavelength combinations  
32 were analysed. The wavelengths with the strongest correlation to seasonal dynamics in ecosystem  
33 properties were shortwave infrared (biomass), the peak absorption band for chlorophyll a and b (at 682  
34 nm) (GPP), the oxygen A-band at 761 nm used for estimating chlorophyll fluorescence (GPP, and  
35 LUE), and blue wavelengths (FAPAR). The NDSI with the strongest correlation to: i) biomass  
36 combined red edge HCRF ( $\rho_{705}$ ) with green HCRF ( $\rho_{587}$ ), ii) GPP combined wavelengths at the peak of  
37 green reflection ( $\rho_{518}, \rho_{556}$ ), iii) the LUE combined red ( $\rho_{688}$ ) with blue HCRF ( $\rho_{436}$ ), and iv) FAPAR  
38 combined blue ( $\rho_{399}$ ) and near infrared ( $\rho_{1295}$ ) wavelengths. NDSI combining near infrared and  
39 shortwave infrared were strongly affected by solar zenith angles and sensor viewing geometry, as were  
40 many combinations of visible wavelengths. This study provides analyses based upon novel multi-  
41 angular hyperspectral data for validation of earth observation based properties of semi-arid ecosystems,  
42 as well as insights for designing spectral characteristics of future sensors for ecosystem monitoring.

## 43 **1. Introduction**

44 Hyperspectral measurements of the Earth's surface provide relevant information for many ecological  
45 applications. An important tool for spatial extrapolation of ecosystem functions and properties is to  
46 study how spectral properties are related to in situ measured ecosystem properties. These relationships  
47 found the basis for up-scaling using earth observation (EO) data. Continuous in situ measurements of  
48 hyperspectral reflectance in combination with ecosystem properties are thereby essential for improving  
49 our understanding of the functioning of the observed ecosystems. Strong relationships have for  
50 example been found between information in the reflectance spectrum and ecosystem properties such as  
51 leaf area index (LAI), fraction of photosynthetically active radiation (PAR) absorbed by the vegetation  
52 (FAPAR), light use efficiency (LUE), biomass, vegetation primary productivity, vegetation water  
53 content, and nitrogen and chlorophyll content (e.g. Thenkabail et al., 2012; Tagesson et al., 2009;  
54 Gower et al., 1999; Sjöström et al., 2009; Sims and Gamon, 2003). In situ observations of spectral  
55 reflectance are also important for parameterisation and validation of canopy reflectance models, and  
56 space and airborne products (Coburn and Peddle, 2006).

57 Very few sites across the world exist with an instrumental setup designed for multi-angular  
58 continuous hyperspectral measurements. Leuning et al. (2006) present a system mounted in a 70 m  
59 tower above an evergreen Eucalyptus forest in New South Wales Australia, which measures spectral  
60 hemispherical conical reflectance factors (HCRF)<sup>1</sup> hourly throughout the year between 300 and 1150  
61 nm at four azimuth angles. Hilker et al. (2007) and Hilker et al. (2010) describe an automated  
62 multiangular spectro-radiometer for estimation of canopy HCRF (AMSPEC) mounted on a tower

---

<sup>1</sup> Different reflectance terminologies have been used to inform on spectral measurements in the field by the remote sensing community leading to suggestions to the proper use of the terminology (Martonchik et al., 2000). All field spectro-radiometers measure HCRF (hemispherical conical reflectance) if the field of view (FOV) of the sensor is larger than 3° (Milton et al., 2009) and is therefore used throughout this paper to support the correct inference and usage of reflectance products (Schaepman-Strub et al., 2006; Milton et al., 2009).

63 above a coniferous forest in Canada. Spectral HCRF is sampled between 350 and 1200 nm year round  
64 under different viewing and sun angle conditions, achieved by collection of data in a near 360° view  
65 around the tower with adjustable viewing zenith angles. Even though in situ measurements of multi-  
66 angular hyperspectral HCRF are fundamental for the EO research community, such datasets are still  
67 rare and at the present state they do not cover different biomes at the global scale (Huber et al., 2014).

68 There are many methods for analysing relationships between hyperspectral reflectance and ecosystem  
69 properties, such as multivariate methods, derivative techniques, and radiative transfer modelling  
70 (Bowyer and Danson, 2004; Ceccato et al., 2002; Danson et al., 1992; Roberto et al., 2012). Still, due  
71 to its simplicity, the combination of reflectance into vegetation indices is the major method for up-  
72 scaling using EO data. By far, the most commonly applied vegetation indices are those based on band  
73 ratios, e.g. the normalised difference vegetation index (NDVI), which is calculated by dividing the  
74 difference in the near infrared (NIR) and red wavelength bands by the sum of the NIR and red bands  
75 (Tucker, 1979; Rouse et al., 1974). The NIR radiance is strongly scattered by the air-water interfaces  
76 between the cells whereas red radiance is absorbed by chlorophyll and its accessory pigments (Gates et  
77 al., 1965). The normalization with the sum in the denominator is a mean to reduce the effects of solar  
78 zenith angle, sensor viewing geometry, and atmospheric errors as well as enhancing the signal of the  
79 observed target (e.g. Qi et al., 1994; Inoue et al., 2008).

80 Wavelength specific spectral reflectance is known to be related to leaf characteristics such as  
81 chlorophyll concentration, dry matter content, internal structure parameters and equivalent water  
82 thickness (Ceccato et al., 2002). Hyperspectral reflectance data can be combined into a matrix of  
83 normalised difference spectral indices (NDSI), following the NDVI rationing approach. Correlating the  
84 NDSI with ecosystem properties provides a way for an improved empirically based understanding of  
85 the relationship between information in the reflectance spectrum with ground surface properties (e.g.

86 Inoue et al., 2008). Several studies have analysed relationships between hyperspectral HCRF, NDSI,  
87 and ecosystem properties (e.g. Thenkabail et al., 2000; Cho et al., 2007; Psomas et al., 2011; Inoue et  
88 al., 2008; Gamon et al., 1992; Feret et al., 2008; Thenkabail et al., 2012). Still, it is extremely important  
89 to examine these relationships for different ecosystems across the earth and investigate their  
90 applicability for different environmental conditions and under different effects of biotic and abiotic  
91 stresses.

92 A strong correlation between an NDSI and an ecosystem property does not necessarily indicate that  
93 the NDSI is a good indicator of vegetation conditions to be applied to EO systems. Visible, NIR and  
94 shortwave infrared (SWIR) have different sensitivity to variations in solar zenith angles, stand  
95 structure, health status of the vegetation, vegetation and soil water content, direct/diffuse radiation  
96 ratio, and sensor viewing geometry. The influence of sun-sensor geometry on the reflected signal has  
97 been studied using radiative transfer models and airborne (e.g. AirMISR) as well as satellite-based  
98 data from instruments such as CHRIS-PROBA, MISR or POLDER (Huber et al., 2010; Maignan et al.,  
99 2004; Javier García-Haro et al., 2006; Jacquemoud et al., 2009; Verhoef and Bach, 2007; Laurent et al.,  
100 2011). However, effects of variable sun angles and sensor viewing geometries are not well documented  
101 in situ for different plant functional types of natural ecosystems except for individual controlled  
102 experiments based on the use of field goniometers (Sandmeier et al., 1998; Schopfer et al., 2008).  
103 Improved knowledge regarding the influence from sun-sensor variability on different NDSI  
104 combinations is thereby essential for validating the applicability of an NDSI for EO up-scaling  
105 purposes.

106 The Dahra field site in Senegal, West Africa, was established in 2002 as an in situ research site to  
107 improve our knowledge regarding properties of semi-arid savanna ecosystems and their responses to  
108 climatic and environmental changes (Tagesson et al., 2015b). A strong focus of this instrumental setup

109 is to gain insight into the relationships between ground surface reflectance and savanna ecosystem  
110 properties for EO up-scaling purposes. This paper presents a unique in situ dataset of seasonal  
111 dynamics in hyperspectral HCRF and demonstrates how it can be used to describe the seasonal  
112 dynamics in ecosystem properties of semi-arid savanna ecosystems. The objectives are threefold: (i) to  
113 quantify the relationship between seasonal dynamics of in situ hyperspectral HCRF between 350 and  
114 1800 nm and ecosystem properties (biomass, gross primary productivity (GPP), LUE, and FAPAR);  
115 (ii) to quantify the relationship between NDSI with different wavelength combinations (350 to 1800  
116 nm) and the measured ecosystem properties; (iii) to analyse and quantify effects of variable sun angles  
117 and sensor viewing geometries on different NDSI combinations.

## 118 **2. Materials and Method**

### 119 **2.1 Site description**

120 All measurements used for the present study were conducted at the Dahra field site in the Sahelian  
121 ecoclimatic zone north-east of the town Dahra in the semi-arid central part of Senegal (15°24'10"N,  
122 15°25'56"W) during 2011 and 2012 (Fig. 1). Rainfall is sparse in the region with a mean annual sum of  
123 416 mm (1951-2003). More than 95% of the rain falls between July and October, with August being  
124 the wettest month. The mean annual air temperature is 29 °C (1951-2003), May is the warmest and  
125 January is the coldest month with mean monthly temperature of 32°C and 25°C, respectively. The  
126 Dahra site has a short growing season (~3 months), following the rainy season with leaf area index  
127 generally ranging between 0 and 2 (Fensholt et al., 2004). South-western winds dominate during the  
128 rainy season and north-eastern winds dominate during the dry season. The area is dominated by annual  
129 grasses (e.g. *Schoenefeldia gracilis*, *Digitaria gayana*, *Dactyloctenium aegypticum*, *Aristida mutabilis*  
130 and *Cenchrus biflorues*) (Mbow et al., 2013) and trees and shrubs (e.g. *Acacia senegalensis* and

131 *Balanites aegyptiaca*) are relatively sparse (~3% of the land cover) (Rasmussen et al., 2011). The  
132 average tree height was 5.2 m and the peak height of the herbaceous layer was 0.7 m (Tagesson et al.,  
133 2015b). A thorough description of the Dahra field site is given in Tagesson et al. (2015b).

134 <Figure 1>

## 135 **2.2 Meteorological and vegetation variables**

136 A range of meteorological variables have been measured in a tower at the Dahra field site for more than  
137 ten years: air temperature (°C) and relative humidity (%) were measured at 2 m height; soil temperature  
138 (°C) and soil moisture (volumetric water content ( $\text{m}^3 \text{m}^{-3} \times 100$ ) (%)) were collected at 0.05m depths;  
139 rainfall (mm) was measured at 2 m height; incoming (<sub>inc</sub>) and reflected (<sub>ref</sub>) PAR ( $\mu\text{mol m}^{-2} \text{s}^{-1}$ ) was  
140 measured at 10.5 m height, and PAR transmitted through the vegetation ( $\text{PAR}_{\text{transmit}}$ ) was measured at 6  
141 plots at ~0.01 m height (Table 1) (Tagesson et al., 2015b). The  $\text{PAR}_{\text{transmit}}$  was measured within 7  
142 meters distance from the tower. PAR absorbed by the vegetation (APAR) was estimated by:

$$143 \text{APAR} = \text{PAR}_{\text{inc}} - \text{PAR}_{\text{ref}} - (1 - \alpha_{\text{soil}}) \times \text{PAR}_{\text{transmit}} \quad (1)$$

144 where  $\alpha_{\text{soil}}$  is the PAR albedo of the soil, which was measured as 0.20 (Tagesson et al., 2015b). FAPAR  
145 was estimated by dividing APAR with  $\text{PAR}_{\text{inc}}$  (Tagesson et al., 2015b). All sensors were connected to a  
146 CR-1000 logger in combination with a multiplexer (Campbell Scientific Inc., North Logan, USA) and  
147 data were sampled every 30 s, and stored as 15 minute averages (sum for rainfall).

148 The total above ground green biomass ( $\text{g m}^{-2}$ ) of the herbaceous vegetation was sampled  
149 approximately every 10 days during the growing seasons 2011 and 2012 at 28 one  $\text{m}^2$  plots located  
150 along two ~1060 m long diagonal transects (Fig. 1f) (Mbow et al., 2013). The method applied was  
151 destructive, so even though the same transects were used for each sampling date, the plots were never  
152 positioned at exactly the same location. The study area is flat and characterised by homogenous

153 grassland savanna and the conditions in these sample plots are generally found to be representative for  
154 the conditions in the entire measurement area (Fensholt et al., 2006). All above ground green  
155 herbaceous vegetation matter was collected and weighed in the field to get the fresh weight. The dry  
156 matter (DW) was estimated by oven-drying the green biomass. For a thorough description regarding  
157 the biomass sampling we refer to Mbow et al. (2013).

158 <Table 1>

### 159 **2.3 Estimates of gross primary productivity and light use efficiency**

160 Net ecosystem exchange of CO<sub>2</sub> (NEE) ( $\mu\text{mol CO}_2 \text{ m}^{-2} \text{ s}^{-1}$ ) was measured with an eddy covariance  
161 system, consisting of an open path infrared gas analyser (LI-7500, LI-COR Inc., Lincoln, USA) and a  
162 3-axis sonic anemometer (Gill instruments, Hampshire, UK) from 18 July 2011 until 31 December  
163 2012 (Table 1). The sensors were mounted 9 m above the ground on a tower (placed 50 m south of the  
164 tower including the meteorological and spectroradiometric sensors) (Fig. 1f). Data were sampled at 20  
165 Hz rate. The post-processing was done with the EddyPro 4.2.1 software (LI-COR Biosciences, 2012),  
166 and statistics were calculated for 30 minute periods. The post-processing includes 2-D coordinate  
167 rotation (Wilczak et al., 2001), time lag removal between anemometer and gas analyser by covariance  
168 maximization (Fan et al., 1990), despiking (Vickers and Mahrt, 1997) (plausibility range: window  
169 average  $\pm 3.5$  standard deviations), linear detrending (Moncrieff et al., 2004), and compensation for  
170 density fluctuations (Webb et al., 1980). Fluxes were also corrected for high pass (Moncrieff et al.,  
171 1997) and low pass filtering effects (Moncrieff et al., 2004). The data were filtered for steady state and  
172 fully developed turbulent conditions, following Foken et al. (2004), and according to statistical tests as  
173 recommended by Vickers and Mahrt (1997). Flux measurements from periods of heavy rainfall were  
174 also removed. For a thorough description of the post processing of the raw eddy covariance data, see  
175 Tagesson et al. (2015a).



176 A possible source of error in a comparison between EC-based variables and spectral HCRF is the  
 177 difference in footprint/ instantaneous field of view (IFOV) between the sensors. The IFOV of the  
 178 spectroradiometer set-up contains only soil and herbaceous vegetation. The footprint of the EC tower  
 179 was estimated using a model based on measurement height, surface roughness and atmospheric  
 180 stability (Hsieh et al., 2000). The median point of maximum contribution is at 69 m, and the median  
 181 70% cumulative flux distance is at 388 m from the tower. The footprint of the EC tower contains semi-  
 182 arid savanna grassland with ~3% tree coverage and the EC data is thereby affected by both woody and  
 183 herbaceous vegetation (Fig. 1a and 1f). But given the low tree coverage, and the dominant influence  
 184 of herbaceous vegetation on the seasonal dynamics in CO<sub>2</sub> fluxes, we still consider it reasonable to  
 185 compare EC fluxes with seasonal dynamics in spectral HCRF of the herbaceous vegetation.

186 The daytime NEE was partitioned to GPP and ecosystem respiration using the Mitscherlich light  
 187 response function against PAR<sub>inc</sub> (Falge et al., 2001). A 7-day moving window with one day time steps  
 188 was used when fitting the functions. By subtracting dark respiration (R<sub>d</sub>) from the light response  
 189 function, it was forced through 0, and GPP was estimated:

$$190 \quad GPP = -(F_{csat} + R_d) \times \left(1 - e^{\left(\frac{-\alpha \times PAR_{inc}}{F_{csat} + R_d}\right)}\right) \quad (2)$$

191 where F<sub>csat</sub> is the CO<sub>2</sub> uptake at light saturation (μmol CO<sub>2</sub> m<sup>-2</sup> s<sup>-1</sup>), and α is the quantum efficiency or  
 192 the initial slope of the light response curve (μmol CO<sub>2</sub> (μmol photons)<sup>-1</sup>) (Falge et al., 2001). Vapor  
 193 pressure deficit (VPD) limits GPP and to account for this effect, the F<sub>csat</sub> parameter was set as an  
 194 exponentially decreasing function:

$$195 \quad F_{csat} = \begin{cases} F_{csat_0} \times e^{-k(VPD - VPD_0)} & VPD > VPD_0 \\ F_{csat_0} & VPD < VPD_0 \end{cases} \quad (3)$$

196 where VPD<sub>0</sub> is 10 hPa following the method by Lasslop et al. (2010).

197 Gaps in GPP less or equal to three days were filled with three different methods: (i) gaps shorter than  
198 two hours were filled using linear interpolation; (ii) daytime gaps were filled by using the light-  
199 response function for the 7-day moving windows; (iii) remaining gaps were filled by using mean  
200 diurnal variation 7-days moving windows (Falge et al., 2001). A linear regression model was fitted  
201 between daytime GPP and APAR for each 7-day moving window to estimate LUE, where LUE is the  
202 slope of the line.

## 203 **2.4 Hyperspectral HCRF measurements and NDSI estimates**

204 Ground surface HCRF spectra were measured every 15 minutes between sunrise and sunset from 15  
205 July 2011 until 31 December 2012 using two FieldSpec3 spectrometers with fiber optic cables (Table  
206 1) (ASD Inc., Colorado, USA). The spectroradiometers cover the spectral range from 350 nm to 1800  
207 nm and have a FOV of 25°. The spectral resolution is 3 nm at 350-1000 nm and 10 nm at 1000-1800  
208 nm and the sampling interval is 1.4 nm at 350-1000 nm and 2 nm at 1000-1800 nm. From these data, 1  
209 nm spectra were calculated by using cubic spline interpolation functions. One sensor head was  
210 mounted on a rotating head 10.5 m above the surface (at the same tower including instruments to  
211 measure meteorological variables) providing measurements of the herbaceous vegetation from seven  
212 different viewing angles in a transect underneath the tower (nadir, 15°, 30°, 45° off-nadir angles  
213 towards east and west). No trees or effects of shading of trees are present in the IFOV of the data used  
214 in this study (Fig. 1). A reflective cosine receptor is used to measure full-sky-irradiance by having the  
215 second sensor head mounted on a 2 m high stand pointing to a Spectralon panel (Labsphere Inc., New  
216 Hampshire, USA) under a glass dome.

217 Each sensor measurement starts with an optimization to adjust the sensitivity of the detectors  
218 according to the specific illumination conditions at the time of measurement. The optimisation is

219 followed by a dark current measurement to account for the noise generated by the thermal electrons  
220 within the ASDs that flows even when no photons are entering the device. The measurement sequence  
221 starts with a full-sky-irradiance measurement, followed by measurements of the 7 angles of the land  
222 surface and finalized by a second full-sky-irradiance measurement. Thirty scans are averaged to one  
223 measurement to improve the signal-to-noise ratio for each measurement (optimisation, dark current,  
224 full-sky irradiance and each of the seven target measurements). The full measurement sequence takes  
225 less than one minute. The two ASD instruments are calibrated against each other before and after each  
226 rainy season. Poor quality measurements caused by unfavorable weather conditions, changing  
227 illumination conditions, irregular technical issues were filtered by comparing full-sky solar irradiance  
228 before and after the target measurements (Huber et al., 2014). The spectral HCRF was derived by  
229 estimating the ratio between the ground surface radiance and full sky irradiance. For a complete  
230 description/illustration of the spectroradiometer set up, the measurement sequence and the quality  
231 control, see Huber et al. (2014).

232 NDSI using all possible combinations of two separate wavelengths were calculated as:

$$233 \quad \text{NDSI} = \frac{(\rho_i - \rho_j)}{(\rho_i + \rho_j)} \quad (4)$$

234 where  $\rho_i$  and  $\rho_j$  are the daily median HCRF in two separate single wavelengths ( $i$  and  $j$ ) between 350  
235 and 1800 nm. In order to minimise the influence of errors we used daily median hyperspectral HCRF in  
236 the analysis (since median provides the most common model output and is thereby more robust against  
237 outliers than average values). NDSI including the water absorption band (1300-1500 nm) was filtered  
238 as it is strongly sensitive to atmospheric water content, and is less suitable for spatial extrapolation of  
239 ecosystem properties using air/space borne sensors (Asner, 1998). Finally, NDSI combinations

240 including wavelengths between 350 and 390 nm were filtered owing to low signal to noise ratio in the  
241 ASD sensors (Thenkabail et al., 2004).

## 242 **2.5 Effects of varying sun and sensor viewing geometry on NDSI**

243 The effects of variable solar zenith angles on different NDSI combinations were studied with nadir  
244 measurements taken over 15 days during the peak of the growing season in 2011 (day of year 237-251).  
245 Only days with full data coverage were used (12 of the 15 days) in order not to include bias in the  
246 results from days with incomplete datasets. The median HCRF of the 15 days was calculated for each  
247 wavelength for every 15 minutes between 8:00 and 18:00. These HCRF values were combined into  
248 NDSI with different wavelength combinations. Finally, daily mean and standard deviation for all  
249 wavelength combinations were calculated. Diurnal variability in the NDSI was assessed with the  
250 coefficient of variation (COV), which is the ratio between the standard deviation and the mean. The  
251 COV gives an indication of effects related to variable solar zenith angles.

252 To capture directional effects in the NDSI related to the variable view zenith angles (15°, 30°, 45°  
253 off-nadir angles towards east and west) the NDSI was calculated using median HCRF values from the  
254 peak of the growing season 2011 (day of year 237-251) for the different viewing angles. Only data  
255 measured between 12:00 and 14:00 was used to avoid effects of variable solar zenith angles. The  
256 anisotropy factor (ANIF) is defined as the fraction of a reflected property at a specific view direction  
257 relative to the nadir, and it was calculated by:

$$258 \text{ANIF}(\lambda, \theta) = \frac{\text{NDSI}(\lambda, \theta)}{\text{NDSI}_0(\lambda)} \quad (5)$$

259 where  $\text{NDSI}(\lambda, \theta)$  is NDSI for the different wavelengths ( $\lambda$ ) and the different viewing angles ( $\theta$ ), and  
260  $\text{NDSI}_0(\lambda)$  is the nadir measured NDSI (Sandmeier et al., 1998).

## 261 **2.6 Relationship between hyperspectral HCRF, NDSI and ecosystem properties**

262 We examined the relationship between predictor variables (daily median hyperspectral HCRF, and  
263 NDSI from nadir observations) and response variables (biomass, GPP, LUE, and FAPAR) using linear  
264 regression analysis. Possible errors (random sampling errors, aerosols, dust or water on the sensor  
265 heads, electrical sensor noise, filtering and gap-filling errors, errors in correction factors, sensor drift,  
266 and instrumentation errors) can be present in predictor and response variables. We thereby used a  
267 reduced major axis linear regression to account for errors in both the predictor and response variables  
268 when fitting the regression lines. In order to estimate the robustness of the empirical relationships, we  
269 used a bootstrap simulation methodology, where the datasets were copied 200 times (Richter et al.,  
270 2012). The runs generated 200 sets of slopes, intercepts, coefficients of determination ( $R^2$ ), from which  
271 median and standard deviation was estimated. The generated statistical models were validated against  
272 the left-out subsamples within the bootstrap simulation method by calculating the root-mean square  
273 error (RMSE) and the relative RMSE ( $RRMSE=100*RMSE*\text{mean}(\text{observed})^{-1}$ ); median and standard  
274 deviation were estimated. Within the regression analysis all variables used were repeated observations  
275 of the same measurement plot. The dependent and independent variables are thereby temporally auto-  
276 correlated and cannot be regarded as statistically independent. We thereby choose not to present any  
277 statistical significance. The analyses, however, still indicate how closely coupled the explanatory  
278 variables are with the ecosystem properties.

279 A filter was created for the analysis between NDSI and ecosystem properties; all NDSI combinations  
280 with a COV higher than 0.066 and all NDSI combinations with ANIF values higher than 1.2 and lower  
281 than 0.8 were filtered. The ANIF threshold of 1.2 and 0.8, and the COV threshold of 0.066 was used  
282 since values then vary less than 20% due to effects of variable sun-sensor geometry.

### 283 3. Results

#### 284 3.1 Seasonal dynamics in meteorological variables, ecosystem properties and 285 hyperspectral HCRF

286 Daily average air temperature at 2 m height ranged between 18.4°C and 37.8°C, with low values during  
287 winter and peak values at the end of the dry season (Fig. 2a). Yearly rainfall was 486 mm and 606 mm  
288 for 2011 and 2012, respectively. Soil moisture ranged between 1.9% and 14.1%, and it clearly followed  
289 the rainfall patterns (Fig. 2b and 2c). The CO<sub>2</sub> fluxes were low during the dry period and high during  
290 the rainy season (July-October) (Fig. 2e). The LUE followed GPP closely (Fig. 2f). FAPAR was low at  
291 the start of the rainy season, followed by a maximum towards the end of the rainy season, and then  
292 slowly decreased over the dry season (Fig. 2g).

293 The range in HCRF is large across the spectral space, and would hide the seasonal dynamics in  
294 hyperspectral HCRF if directly shown. Therefore, to clearly illustrate the seasonal dynamics in  
295 hyperspectral HCRF, the ratio between daily median nadir HCRF and the average HCRF for the entire  
296 measurement period was calculated for each wavelength (350-1800 nm). This gives a fraction of how  
297 the HCRF for each wavelength varies over the measurement period in relation to the average of the  
298 entire period (Fig. 2d). In the visible (VIS) part of the spectrum (350-700 nm) there was a stronger  
299 absorption during the second half of the rainy season and at the beginning of the dry season than during  
300 the main part of the dry season and the start of the rainy season. There was stronger NIR absorption  
301 (700-1300 nm) at the end of the rainy season and the beginning of the dry season, whereas the  
302 absorption decreased along with the dry season. Strong seasonal variation was observed in the water  
303 absorption region around 1400 nm following the succession of rainy and dry seasons. HCRF in the  
304 short-wave infrared (SWIR; 1400-1800 nm) generally followed the seasonal dynamics of the visible  
305 part of the spectrum.

306 <Figure 2>

### 307 **3.2 Effects of sensor viewing geometry and variable sun angles on NDSI**

308 The most pronounced effects of solar zenith angles at the peak of the growing season 2011 were  
309 observed for NDSI combining SWIR and NIR wavelengths, and with VIS wavelengths between 550  
310 nm and 700 nm (n=576) (Fig. 3). Remaining VIS wavelengths were mostly affected by solar zenith  
311 angles when combined with the water absorption wavelengths around 1400 nm. The same effects were  
312 seen for the view zenith angles; the strongest effects were seen for NDSI with SWIR and NIR  
313 combinations, and VIS wavelengths between 550 and 700 nm (Fig. 4). Remaining VIS wavelengths  
314 were less affected. It was also clear that ground surface anisotropy increased strongly as a function of  
315 increasing viewing angle (Fig. 4). Moreover, some band combinations showed already angular  
316 sensitivity at view zenith angles of 15 °, while other band combinations only manifest anisotropic  
317 behaviour with higher view angles. Some band combinations, however, do not show any increased  
318 anisotropy at all (areas coloured in green in all three plots).

319 <Figure 3>

320 <Figure 4>

### 321 **3.3 Relationship between hyperspectral HCRF, NDSI and ecosystem properties**

#### 322 **3.3.1 Biomass**

323 HCRF values for all wavelengths except the water absorption band at 1100 nm were strongly correlated  
324 to biomass (Fig. 5a). The strongest correlation was found at  $\rho_{1675}$  (median $\pm$  1 standard deviation;  $r=-$   
325  $0.88\pm 0.09$ ), but biomass was almost equally well correlated to blue, red and NIR wavelengths. All  
326 presented correlations and relationships throughout the text are based on filtered data. Negative  
327 correlations indicate that the more biomass the higher the absorption and hence the lower the HCRF. A

328 small peak of positive correlation is seen at 1120-1150 nm caused by a water absorption peak around  
329 this wavelength (Thenkabail et al., 2012). NDSI combinations with HCRF in the red edge ( $\rho_{680-750}$ )  
330 and HCRF in the VIS region explained seasonal dynamics in biomass well (Fig. 6a). The strongest  
331 relationship ( $R^2=0.88\pm 0.07$ ;  $RRMSE=18.6\pm 5.7\%$ ) between NDSI and biomass was found for NDSI  
332 combining 705 and 587 nm (NDSI[705, 587]) (Table 2, Fig. 7a).

### 333 **3.3.2 Gross primary productivity**

334 The relationship between GPP and nadir measured hyperspectral HCRF is inverted as compared to  
335 other correlation coefficient lines (Fig. 5b), since GPP is defined as a withdrawal of CO<sub>2</sub> from the  
336 atmosphere with higher negative values for a larger CO<sub>2</sub> uptake. The seasonal dynamics in GPP was  
337 strongly positively correlated to HCRF in the blue, red, SWIR wavelengths, and the water absorption  
338 band at 1100 nm whereas it was strongly negatively correlated to the NIR HCRF. The study revealed  
339 the strongest positive and negative correlations for HCRF at 682 nm ( $r=0.70\pm 0.02$ ) and 761 nm ( $r=-$   
340  $0.74\pm 0.02$ ), respectively. NDSI combinations that explained most of the GPP variability were different  
341 combinations of the VIS and NIR or red and SWIR wavelengths (Fig. 6b). However, the strongest  
342 relationship was seen at NDSI[518, 556] ( $R^2=0.86\pm 0.02$ ;  $RRMSE=34.9\pm 2.3\%$ ) (Table 2; Fig. 7b).

### 343 **3.3.3 Light use efficiency**

344 LUE was negatively correlated with HCRF in the blue, and red spectral ranges and in the water  
345 absorption band at 1100 nm and it was positively correlated in the NIR wavelengths (Fig. 5c). HCRF at  
346 761 nm yielded the strongest positive correlation ( $r=0.87\pm 0.01$ ). When combining the different  
347 wavelengths to NDSI, the VIS wavelengths explained variation in LUE well, with the strongest  
348 relationships in the red and blue parts of the spectrum (Fig. 6c). LUE correlated most strongly with  
349 NDSI[436, 688] ( $R^2=0.81\pm 0.02$ ;  $RRMSE=52.8\pm 3.8\%$ ) (Table 2; Fig. 7c).



350 **3.3.4 Fraction of photosynthetically active radiation absorbed by the vegetation**

351 FAPAR was negatively correlated to nadir measured HCRF for most wavelengths (Fig. 5d); the higher  
352 FAPAR the higher the absorption, and thereby the lower the HCRF. The strongest correlation was  
353 found at a blue wavelength  $\rho_{412}$  ( $r=-0.92\pm0.01$ ). When wavelengths were combined to NDSI,  
354 combining violet/blue with NIR and SWIR wavelengths generated the NDSI with the strongest  
355 relationships (Fig. 6d) with a maximum  $R^2$  of  $0.81\pm0.02$  (RRMSE= $14.6\pm0.7$  %) for NDSI[399, 1295]  
356 (Table 2; Fig. 7d).

357 <Table 2>

358 <Figure 5>

359 <Figure 6>

360 <Figure 7>

361 **4. Discussion**

362 **4.1 Effects of sensor viewing geometry and variable sun angles on the NDSI**

363 Effects of solar zenith angles and sensor viewing geometry were similar (Fig. 3 and 4), since they  
364 affect HCRF measurements in a similar way (Kimes, 1983). In dense and erectophile canopies, HCRF  
365 increases with sensor viewing and solar zenith angles, because a larger fraction of the upper vegetation  
366 canopy is viewed/illuminated, whereas the shadowed lower part of the canopy contributes less to the  
367 measured signal as shown previously by several studies (Huete et al., 1992; Jin et al., 2002; Huber et  
368 al., 2014; Kimes, 1983). However, the radiative transfer within a green canopy is complex, and differs  
369 across the spectral region (Huber et al., 2014). Less radiation is available for scattering of high  
370 absorbing spectral ranges (such as the VIS wavelengths), and this tends to increase the contrast  
371 between shadowed and illuminated areas for these wavelengths, whereas in the NIR and SWIR ranges,

372 more radiation is scattered and transmitted, which thereby decreases the difference between shadowed  
373 and illuminated areas within the canopy (Kimes, 1983; Hapke et al., 1996). A recognised advantage of  
374 NDSI calculations is that errors/biases being similar in both wavelengths included in the index are  
375 suppressed by the normalisation. However, for a given situation where errors/biases are different for  
376 the wavelengths used, such as effects generated by sun-sensor geometry, it will affect the value of the  
377 index. This was also the case at the Dahra field site: NDSI values were strongly affected at wavelength  
378 combinations with large differences in effects of variable solar zenith angles (Fig. 6 in Huber et al.  
379 (2014)) and at wavelength combinations with large differences in effects related to the variable view  
380 zenith angles (Fig. 4 in Tagesson et al. (2015b)). This effect is especially pronounced in the case for  
381 low index values (closer to 0) whereas larger index values (closer to 1 and -1) become less sensitive.  
382 The relative HCRF difference between NIR and SWIR is lower as compared to indices including the  
383 VIS domain; NIR/SWIR based indices thereby generate lower NDSI values with higher sensitivity to  
384 sun-sensor geometry generated differences between included wavelengths (Fig. 3 and 4).

385 The importance of directional effects for the applicability of normalized difference spectral indices  
386 has been pointed out as an issue in numerous papers (e.g. Holben and Fraser, 1984; van Leeuwen et al.,  
387 1999; Cihlar et al., 1994; Fensholt et al., 2010; Gao et al., 2002). This study confirms these challenges  
388 for NIR/SWIR based indices, but the results also indicate several wavelength combinations from which  
389 these effects are less severe and potentially applicable to EO data without disturbance from  
390 viewing/illumination geometry for this type of vegetation. Multi-angular HCRF data provide additional  
391 information of e.g. canopy structure, photosynthetic efficiency and capacity (Bicheron and Leroy,  
392 2000; Asner, 1998; Pisek et al., 2013; Huber et al., 2010), and this unique in situ based multi-angular  
393 high temporal resolution dataset may thus be used for future research of canopy radiative transfer and  
394 BRDF (bidirectional reflectance distribution function) modelling (Jacquemoud et al., 2009; Bicheron

395 and Leroy, 2000). The multi-angular dataset is also highly valuable for evaluation and validation of  
396 satellite based products, where the separation of view angle and atmospheric effects can only be done  
397 using radiative transfer models (Holben and Fraser, 1984).

## 398 **4.2 Seasonal dynamics in hyperspectral HCRF, NDSI and ecosystem properties**

### 399 **4.2.1 Biomass**

400 The strong correlation between biomass and most of the spectrum indicates the strong effects of  
401 phenology on the seasonal dynamics in the HCRF spectra (Fig. 5a). Variability in VIS (350-700 nm)  
402 HCRF for vegetated areas is strongly related to changes in leaf pigments (Asner, 1998), and this can  
403 also be seen in Fig. 2d since absorption was much stronger during the rainy (growing) season, than  
404 during the dry season. Previous studies have generally shown positive relationships between NIR  
405 HCRF and biomass since a large fraction of NIR radiation is reflected in green healthy vegetation to  
406 avoid overheating (e.g. Hansen and Schjoerring, 2003; Asner, 1998). Here, a strong negative  
407 relationship between NIR HCRF and dry weight biomass is generally observed (Fig. 5a), whereas a  
408 strong positive NIR HCRF correlation with vegetation water content was seen (figure not shown). This  
409 is interesting and should be studied further to better understand the respective importance of canopy  
410 water and leaf internal cellular structure for the NIR HCRF of herbaceous vegetation characterised by  
411 erectophile leaf angle distribution (LAD). We found the strongest correlation for biomass with a SWIR  
412 wavelength thereby confirming the studies by Lee (2004) and Psomas et al. (2011) in that SWIR  
413 wavelengths are good predictors of LAI or biomass.

414 The NDVI is known to saturate at high biomass because the absorption of red light at ~680 nm  
415 saturates at higher biomass loads whereas the NIR HCRF continues to increase due to multiple  
416 scattering effects (Mutanga and Skidmore, 2004; Jin and Eklundh, 2014). Several studies have shown

417 that NDSI computed with narrowband HCRF improve this relationship by choosing a wavelength  
418 region not as close to the maximum red absorption at ~680 nm, for example using shorter and longer  
419 wavelengths of the red edge (700 - 780nm) (Cho et al., 2007; Mutanga and Skidmore, 2004; Lee,  
420 2004), and NIR and SWIR wavelengths (Psomas et al., 2011; Lee, 2004). The NDSI with the strongest  
421 correlation to biomass was computed using red edge HCRF ( $\rho_{705}$ ) and green HCRF ( $\rho_{587}$ ). Vegetation  
422 stress and information about chlorophyll and nitrogen status of plants can be extracted from the red-  
423 edge region (Gitelson et al., 1996). Wavelengths around  $\rho_{550}$  are located right at the peak of green  
424 reflection and closely related to the total chlorophyll content, leaf nitrogen content, and  
425 chlorophyll/carotenoid ratio and have previously been shown to be closely related to biomass (Inoue et  
426 al., 2008; Thenkabail et al., 2012).

#### 427 **4.2.2 Gross primary productivity**

428 The maximum absorption in the red wavelengths generally occurs at 682 nm as this is the peak  
429 absorption for chlorophyll a and b (Thenkabail et al., 2000), and this was also the wavelength being  
430 most strongly correlated with GPP. HCRF at 682 nm was previously shown to be strongly related to  
431 LAI, biomass, plant height, NPP, and crop type discrimination (Thenkabail et al., 2004; Thenkabail et  
432 al., 2012). The NDSI with the strongest relationship to GPP was based on HCRF in the vicinity of the  
433 green peak. The photochemical reflectance index (PRI) normalizes HCRF at 531 nm and 570 nm and it  
434 was suggested for detection of diurnal variation in the xanthophyll cycle activity (Gamon et al., 1992),  
435 and it is commonly used for estimating productivity efficiency of the vegetation (e.g. Soudani et al.,  
436 2014). The present study thereby confirms the strong applicability of the wavelengths in the vicinity of  
437 the green peak for vegetation productivity studies. Again, wavelengths around the green peak are

438 related to the total chlorophyll content, leaf nitrogen content, chlorophyll/carotenoid ratio, and biomass  
439 (Inoue et al., 2008; Thenkabail et al., 2012).

#### 440 **4.2.3 Light use efficiency**

441 Both LUE and GPP were most strongly correlated with HCRF at 761 nm, which is the oxygen A-band  
442 within the NIR wavelengths. HCRF at 761 nm is commonly used for estimating solar-induced  
443 chlorophyll fluorescence due to radiation emitted by the chlorophyll, and it has been suggested as a  
444 direct measure of health status of the vegetation (Meroni et al., 2009). Earth observation data for  
445 estimating fluorescence should have very high spectral resolution (<10 nm) due to its narrow features,  
446 but considering the rapid technical development within sensors for hyperspectral measurements,  
447 fluorescence possibly has strong practical potential for monitoring vegetation status (Meroni et al.,  
448 2009; Entcheva Campbell et al., 2008). Globally mapped terrestrial chlorophyll fluorescence retrievals  
449 are already produced from the GOME-2 instrument at a spatial resolution of  $0.5^{\circ} \times 0.5^{\circ}$ , but hopefully  
450 this will be available also with EO sensors of higher spatial and temporal resolution in the future  
451 (Joiner et al., 2013).

452 The strongest wavelength combinations for estimating LUE for this semi-arid ecosystem was  
453 NDSI[688, 435]. The 688 nm wavelength is just at the base of the red edge region, again indicating the  
454 importance of this spectral region for estimating photosynthetic activity. The wavelength at 435 nm is  
455 at the center of the blue range characterized by chlorophyll utilization, and strongly related to  
456 chlorophyll a and b, senescing, carotenoid, loss of chlorophyll, and vegetation browning (Thenkabail et  
457 al., 2004; Thenkabail et al., 2012). The NDSI[688, 435] thereby explores the difference between  
458 information about chlorophyll content and information about senescence of the canopy, which should  
459 be a good predictor of ecosystem level photosynthetic efficiency.

#### 460 **4.2.4 Fraction of photosynthetically active radiation absorbed by the vegetation**

461 FAPAR is an estimate of radiation absorption in the photosynthetically active spectrum and thereby  
462 strongly negatively correlated to most parts of the spectrum (Fig. 5d). FAPAR remained high during  
463 the dry season because of standing dry biomass that was slowly degrading over the dry season (Fig.  
464 2g). The seasonal dynamics in FAPAR is thereby strongly related to senescence of the vegetation,  
465 which explains why FAPAR was most strongly correlated to blue wavelengths ( $\rho_{412}$ ). Several studies  
466 reported a strong relationship between NDVI and FAPAR (e.g. Tagesson et al., 2012; Myneni and  
467 Williams, 1994; Fensholt et al., 2004), but this relationship has been shown to vary for the vegetative  
468 phase and the periods of senescence (Inoue et al., 1998; Tagesson et al., 2015b). As showed by Inoue et  
469 al. (2008), and confirmed by this study, new indices combining blue with NIR wavelengths could be  
470 used for estimating FAPAR for the entire phenological cycle. This result has implications for studies  
471 using the LUE approach for estimating C assimilations (Hilker et al., 2008).

#### 472 **4.3 Outlook and perspectives**

473 Very limited multi-angular hyperspectral in situ data exists, even though it has been, and will continue  
474 to be extremely valuable for an improved understanding of the interaction between ground surface  
475 properties and radiative transfer. In this study, we have presented a unique in situ dataset of multi-  
476 angular, high temporal resolution hyperspectral HCRF (350-1800 nm) and demonstrated the  
477 applicability of hyperspectral data for estimating ground surface properties of semi-arid savanna  
478 ecosystems using NDSI. The study was conducted in spatially homogeneous savanna grassland,  
479 suggesting that the results should be commonly applicable for this biome type. However, attention  
480 should be paid to site-specific details that could affect the indices, such as species composition, soil  
481 type, biotic and abiotic stresses, and stand structure. Additionally, the biophysical mechanisms behind

482 the NDSIs are not well understood at the moment, and further studies are needed to examine the  
483 applicability of these indices to larger regions and other ecosystems. Being a 2-band ratio approach,  
484 NDSI does not take full advantage of exploring the rich information given by the hyperspectral HCRF  
485 measurements. In the future, this hyperspectral HCRF data-set could be fully explored using e.g.  
486 derivative techniques, multivariate methods, and creation, parameterisation and evaluation of BRDF  
487 and radiative transfer models.

488 Even though several other methods exist which fully exploit the information in the hyperspectral  
489 spectrum, results of the present study still indicate the strength of normalised difference indices for  
490 extrapolating seasonal dynamics in properties of savanna ecosystems. A number of wavelengths  
491 spectra that are highly correlated to seasonal dynamics in properties of semiarid savanna ecosystems  
492 have been identified. The relationships between NDSI and ecosystem properties were better  
493 determined, or at the same level, as results of previous studies exploring relationships between  
494 hyperspectral reflectance and ecosystem properties (Kumar, 2007; Cho et al., 2007; Mutanga and  
495 Skidmore, 2004; Psomas et al., 2011; Ide et al., 2010). By studying also the impact from varying  
496 viewing and illumination geometry the feasibility and applicability of using indices for up-scaling to  
497 EO data was evaluated. As such, the results presented here offer insights for assessment of ecosystem  
498 properties using EO data and this information could be used for designing future sensors for  
499 observation of ecosystem properties of the Earth.

500 **Acknowledgements**

501 This paper was written within the frame of the project entitled Earth Observation based Vegetation  
502 productivity and Land Degradation Trends in Global Drylands. The project was funded by the Danish  
503 Council for Independent Research (DFF) Sapere Aude programme. The site is maintained by the  
504 Centre de Recherches Zootechniques de Dahra, Institut Sénégalais de Recherches Agricoles (ISRA).

505

506



507 **References**

- 508 Asner, G. P.: Biophysical and Biochemical Sources of Variability in Canopy Reflectance, *Remote*  
509 *Sens. Environ.*, 64, 234-253, [http://dx.doi.org/10.1016/S0034-4257\(98\)00014-5](http://dx.doi.org/10.1016/S0034-4257(98)00014-5), 1998.
- 510 Bicheron, P., and Leroy, M.: Bidirectional reflectance distribution function signatures of major biomes  
511 observed from space, *J. Geophys. Res. -Atmos.*, 105, 26669-26681, 10.1029/2000JD900380, 2000.
- 512 Bowyer, P., and Danson, F. M.: Sensitivity of spectral reflectance to variation in live fuel moisture  
513 content at leaf and canopy level, *Remote Sens. Environ.*, 92, 297-308,  
514 <http://dx.doi.org/10.1016/j.rse.2004.05.020>, 2004.
- 515 Ceccato, P., Gobron, N., Flasse, S., Pinty, B., and Tarantola, S.: Designing a spectral index to estimate  
516 vegetation water content from remote sensing data: Part 1: Theoretical approach, *Remote Sens.*  
517 *Environ.*, 82, 188-197, [http://dx.doi.org/10.1016/S0034-4257\(02\)00037-8](http://dx.doi.org/10.1016/S0034-4257(02)00037-8), 2002.
- 518 Cho, M. A., Skidmore, A., Corsi, F., van Wieren, S. E., and Sobhan, I.: Estimation of green grass/herb  
519 biomass from airborne hyperspectral imagery using spectral indices and partial least squares regression,  
520 *Int. J. Appl. Earth Obs. Geoinf.*, 9, 414-424, <http://dx.doi.org/10.1016/j.jag.2007.02.001>, 2007.
- 521 Cihlar, J., Manak, D., and Voisin, N.: AVHRR bidirectional reflectance effects and compositing,  
522 *Remote Sens. Environ.*, 48, 77-88, [http://dx.doi.org/10.1016/0034-4257\(94\)90116-3](http://dx.doi.org/10.1016/0034-4257(94)90116-3), 1994.
- 523 Coburn, C. A., and Peddle, D. R.: A low-cost field and laboratory goniometer system for estimating  
524 hyperspectral bidirectional reflectance, *Can. J. Remote Sens.*, 32, 244-253, 10.5589/m06-021, 2006.
- 525 Danson, F. M., Steven, M. D., Malthus, T. J., and Clark, J. A.: High-spectral resolution data for  
526 determining leaf water content, *Int. J. Remote Sens.*, 13, 461-470, 10.1080/01431169208904049, 1992.
- 527 Entcheva Campbell, P. K., Middleton, E. M., Corp, L. A., and Kim, M. S.: Contribution of chlorophyll  
528 fluorescence to the apparent vegetation reflectance, *Sci. Total Environ.*, 404, 433-439,  
529 <http://dx.doi.org/10.1016/j.scitotenv.2007.11.004>, 2008.
- 530 Falge, E., Baldocchi, D., Olson, R., Anthoni, P., Aubinet, M., Bernhofer, C., Burba, G., Ceulemans, R.,  
531 Clement, R., Dolman, H., Granier, A., Gross, P., Grunwald, T., Hollinger, D., Jensen, N. O., Katul, G.,  
532 Keronen, P., Kowalski, A., Lai, C. T., Law, B. E., Meyers, T., Moncrieff, J., Moors, E., Munger, J. W.,  
533 Pilegaard, K., Rannik, U., Rebmann, C., Suyker, A., Tenhunen, J., Tu, K., Verma, S., Vesala, T.,  
534 Wilson, K., and Wofsy, S.: Gap filling strategies for defensible annual sums of net ecosystem  
535 exchange, *Agric. For. Meteorol.*, 107, 43-69, 2001.
- 536 Fan, S. M., Wofsy, S. C., Bakwin, P. S., Jacob, D. J., and Fitzjarrald, D. R.: Atmosphere-Biosphere  
537 Exchange of CO<sub>2</sub> and O<sub>3</sub> in the Central Amazon Forest, *J. Geophys. Res.*, 95, 16851-16864, 1990.
- 538 Fensholt, R., Sandholt, I., and Rasmussen, M. S.: Evaluation of MODIS LAI, fAPAR and the relation  
539 between fAPAR and NDVI in a semi-arid environment using in situ measurements, *Remote Sens.*  
540 *Environ.*, 91, 490-507, <http://dx.doi.org/10.1016/j.rse.2004.04.009>, 2004.
- 541 Fensholt, R., Sandholt, I., and Stisen, S.: Evaluating MODIS, MERIS, and VEGETATION vegetation  
542 indices using in situ measurements in a semiarid environment, *IEEE T. Geosci. Remote*, 44, 1774-  
543 1786, 10.1109/TGRS.2006.875940, 2006.
- 544 Fensholt, R., Sandholt, I., Proud, S. R., Stisen, S., and Rasmussen, M. O.: Assessment of MODIS sun-  
545 sensor geometry variations effect on observed NDVI using MSG SEVIRI geostationary data, *Int. J.*  
546 *Remote Sens.*, 31, 6163-6187, 2010.
- 547 Feret, J.-B., François, C., Asner, G. P., Gitelson, A. A., Martin, R. E., Bidel, L. P. R., Ustin, S. L., le  
548 Maire, G., and Jacquemoud, S.: PROSPECT-4 and 5: Advances in the leaf optical properties model  
549 separating photosynthetic pigments, *Remote Sens. Environ.*, 112, 3030-3043,  
550 <http://dx.doi.org/10.1016/j.rse.2008.02.012>, 2008.

551 Foken, T., Gøckede, M., Mauder, M., Mahrt, L., Amiro, B., and Munger, W.: Post-field data quality  
552 control, in: Handbook of Micrometeorology- A guidebook for Surface Flux Measurement and Analysis,  
553 edited by: Lee, J. A., Massman, W., and Law, B., Kluwer Academic Publishers, London, 181-203,  
554 2004.

555 Gamon, J. A., Peñuelas, J., and Field, C. B.: A narrow-waveband spectral index that tracks diurnal  
556 changes in photosynthetic efficiency, *Remote Sens. Environ.*, 41, 35-44,  
557 [http://dx.doi.org/10.1016/0034-4257\(92\)90059-S](http://dx.doi.org/10.1016/0034-4257(92)90059-S), 1992.

558 Gao, F., Jin, Y., Schaaf, C. B., and Strahler, A. H.: Bidirectional NDVI and atmospherically resistant  
559 BRDF inversion for vegetation canopy, *IEEE Transactions on Geoscience and Remote Sensing*, 40,  
560 1269-1278, 10.1109/TGRS.2002.800241, 2002.

561 Gates, D. M., Keegan, H. J., Schleter, J. C., and Weidner, V. R.: Spectral Properties of Plants, *Appl.*  
562 *Optics*, 4, 11-20, 1965.

563 Gitelson, A. A., Merzlyak, M. N., and Lichtenthaler, H. K.: Detection of Red Edge Position and  
564 Chlorophyll Content by Reflectance Measurements Near 700 nm, *J. Plant Physiol.*, 148, 501-508,  
565 [http://dx.doi.org/10.1016/S0176-1617\(96\)80285-9](http://dx.doi.org/10.1016/S0176-1617(96)80285-9), 1996.

566 Gower, S. T., Kucharik, C. J., and Norman, J. M.: Direct and indirect estimation of leaf area index,  
567 fAPAR, and net primary production of terrestrial ecosystems - a real or imaginary problem?, *Remote*  
568 *Sens. Environ.*, 70, 29-51, 1999.

569 Hansen, P. M., and Schjoerring, J. K.: Reflectance measurement of canopy biomass and nitrogen status  
570 in wheat crops using normalized difference vegetation indices and partial least squares regression,  
571 *Remote Sens. Environ.*, 86, 542-553, [http://dx.doi.org/10.1016/S0034-4257\(03\)00131-7](http://dx.doi.org/10.1016/S0034-4257(03)00131-7), 2003.

572 Hapke, B., DiMucci, D., Nelson, R., and Smythe, W.: The cause of the hot spot in vegetation canopies  
573 and soils: Shadow-hiding versus coherent backscatter, *Remote Sens. Environ.*, 58, 63-68,  
574 [http://dx.doi.org/10.1016/0034-4257\(95\)00257-X](http://dx.doi.org/10.1016/0034-4257(95)00257-X), 1996.

575 Hilker, T., Coops, N. C., Nestic, Z., Wulder, M. A., and Black, A. T.: Instrumentation and approach for  
576 unattended year round tower based measurements of spectral reflectance, *Computers and Electronics in*  
577 *Agriculture*, 56, 72-84, 10.1016/j.compag.2007.01.003, 2007.

578 Hilker, T., Coops, N. C., Wulder, M. A., Black, T. A., and Guy, R. D.: The use of remote sensing in  
579 light use efficiency based models of gross primary production: A review of current status and future  
580 requirements, *Sci. Total Environ.*, 404, 411-423, <http://dx.doi.org/10.1016/j.scitotenv.2007.11.007>,  
581 2008.

582 Hilker, T., Nestic, Z., Coops, N. C., and Lessard, D.: A new automated, multiangular radiometer  
583 instrument for tower-based observations of canopy reflectance (AMSPEC II), *Instrumentation Science*  
584 *& Technology*, 38, 319-340, 10.1080/10739149.2010.508357, 2010.

585 Holben, B., and Fraser, R. S.: Red and near-infrared sensor response to off-nadir viewing, *Int. J.*  
586 *Remote Sens.*, 5, 145-160, 10.1080/01431168408948795, 1984.

587 Hsieh, C. I., Katul, G., and Chi, T. W.: An approximate analytical model for footprint estimation of  
588 scalar fluxes in thermally stratified atmospheric flows, *Adv. Water Res.*, 23, 765-772, 2000.

589 Huber, S., Koetz, B., Psomas, A., Kneubuehler, M., Schopfer, J. T., Itten, K. I., and Zimmermann, N.  
590 E.: Impact of multiangular information on empirical models to estimate canopy nitrogen concentration  
591 in mixed forest, *APPRES*, 4, 043530-043530-043517, 10.1117/1.3435334, 2010.

592 Huber, S., Tagesson, T., and Fensholt, R.: An automated field spectrometer system for studying VIS,  
593 NIR and SWIR anisotropy for semi-arid savanna, *Remote Sens. Environ.*, 152, 547-556, 2014.

594 Huete, A. R., Hua, G., Qi, J., Chehbouni, A., and van Leeuwen, W. J. D.: Normalization of  
595 multidirectional red and NIR reflectances with the SAVI, *Remote Sens. Environ.*, 41, 143-154,  
596 [http://dx.doi.org/10.1016/0034-4257\(92\)90074-T](http://dx.doi.org/10.1016/0034-4257(92)90074-T), 1992.

597 Ide, R., Nakaji, T., and Oguma, H.: Assessment of canopy photosynthetic capacity and estimation of  
598 GPP by using spectral vegetation indices and the light-response function in a larch forest, *Agric. For.*  
599 *Meteorol.*, 150, 389-398, 2010.

600 Inoue, Y., Moran, M. S., and Horie, T.: Analysis of spectral measurements in rice paddies for  
601 predicting rice growth and yield based on a simple crop simulation model, *Plant Production Science*, 1,  
602 269–279, 1998.

603 Inoue, Y., Penuelas, J., Miyata, A., and Mano, M.: Normalized difference spectral indices for  
604 estimating photosynthetic efficiency and capacity at a canopy scale derived from hyperspectral and  
605 CO<sub>2</sub> flux measurements in rice, *Remote Sens. Environ.*, 112, 156-172, 2008.

606 Jacquemoud, S., Verhoef, W., Baret, F., Bacour, C., Zarco-Tejada, P. J., Asner, G. P., François, C., and  
607 Ustin, S. L.: PROSPECT+SAIL models: A review of use for vegetation characterization, *Remote Sens.*  
608 *Environ.*, 113, Supplement 1, S56-S66, <http://dx.doi.org/10.1016/j.rse.2008.01.026>, 2009.

609 Javier García-Haro, F., Camacho-de Coca, F., and Meliá, J.: Retrieving leaf area index from multi-  
610 angular airborne data, *Annals of Geophysics*, 49, 209-218, 2006.

611 Jin, H., and Eklundh, L.: A physically based vegetation index for improved monitoring of plant  
612 phenology, *Remote Sens. Environ.*, 152, 512-525, <http://dx.doi.org/10.1016/j.rse.2014.07.010>, 2014.

613 Jin, Y., Gao, F., Schaaf, C. B., Xiaowen, L., Strahler, A. H., Bruegge, C. J., and Martonchik, J. V.:  
614 Improving MODIS surface BRDF/Albedo retrieval with MISR multiangle observations, *IEEE T.*  
615 *Geosci. Remote*, 40, 1593-1604, 10.1109/TGRS.2002.801145, 2002.

616 Joiner, J., Guanter, L., Lindstrot, R., Voigt, M., Vasilkov, A. P., Middleton, E. M., Huemmrich, K. F.,  
617 Yoshida, Y., and Frankenberg, C.: Global monitoring of terrestrial chlorophyll fluorescence from  
618 moderate-spectral-resolution near-infrared satellite measurements: methodology, simulations, and  
619 application to GOME-2, *Atmospheric Measuring Techniques*, 6, 2803-2823, doi:10.5194/amt-6-2803-  
620 2013, 2013.

621 Kimes, D. S.: Dynamics of Directional Reflectance Factor Distributions for Vegetation Canopies,  
622 *Appl. Optics*, 22, 1364-1372, 1983.

623 Kumar, L.: High-spectral resolution data for determining leaf water content in Eucalyptus species: leaf  
624 level experiments, *Geocarto International*, 22, 3-16, 2007.

625 Lasslop, G., Reichstein, M., and Papale, D.: Separation of net ecosystem exchange into assimilation  
626 and respiration using a light response curve approach: critical issues and global evaluation, *Global*  
627 *Change Biol.*, 16, 187-209, 2010.

628 Laurent, V. C. E., Verhoef, W., Clevers, J. G. P. W., and Schaepman, M. E.: Inversion of a coupled  
629 canopy–atmosphere model using multi-angular top-of-atmosphere radiance data: A forest case study,  
630 *Remote Sens. Environ.*, 115, 2603-2612, <http://dx.doi.org/10.1016/j.rse.2011.05.016>, 2011.

631 Lee, K., Cohen, WB, Kennedy, RE, Maersperger, TK, Gower, ST Hyperspectral versus multispectral  
632 data for estimating leaf area index in four different biomes, *Remote Sens. Environ.*, 91, 508-520, 2004.

633 Leuning, R., Hughes, D., Daniel, P., Coops, N. C., and Newnham, G.: A multi-angle spectrometer for  
634 automatic measurement of plant canopy reflectance spectra, *Remote Sens. Environ.*, 103, 236-245,  
635 10.1016/j.rse.2005.06.016, 2006.

636 LI-COR Biosciences: EDDYPRO Eddy Covariance Software Version 4.0 User's Guide & Reference,  
637 LI-COR Inc., Lincoln, 200 pp., 2012.

638 Maignan, F., Bréon, F. M., and Lacaze, R.: Bidirectional reflectance of Earth targets: evaluation of  
639 analytical models using a large set of spaceborne measurements with emphasis on the Hot Spot,  
640 *Remote Sens. Environ.*, 90, 210-220, <http://dx.doi.org/10.1016/j.rse.2003.12.006>, 2004.

641 Martonchik, J. V., Bruegge, C. J., and Strahler, A. H.: A review of reflectance nomenclature used in  
642 remote sensing, *Remote Sensing Reviews*, 19, 9-20, 10.1080/02757250009532407, 2000.

643 Mbow, C., Fensholt, R., Rasmussen, K., and Diop, D.: Can vegetation productivity be derived from  
644 greenness in a semi-arid environment? Evidence from ground-based measurements, *J. Arid Environ.*,  
645 97, 56-65, <http://dx.doi.org/10.1016/j.jaridenv.2013.05.011>, 2013.

646 Meroni, M., Rossini, M., Guanter, L., Alonso, L., Rascher, U., Colombo, R., and Moreno, J.: Remote  
647 sensing of solar-induced chlorophyll fluorescence: Review of methods and applications, *Remote Sens.*  
648 *Environ.*, 113, 2037-2051, <http://dx.doi.org/10.1016/j.rse.2009.05.003>, 2009.

649 Milton, E. J., Schaepman, M. E., Anderson, K., Kneubühler, M., and Fox, N.: Progress in field  
650 spectroscopy, *Remote Sens. Environ.*, 113, Supplement 1, S92-S109,  
651 <http://dx.doi.org/10.1016/j.rse.2007.08.001>, 2009.

652 Moncrieff, J. B., Massheder, J. M., de Bruin, H., Elbers, J., Friborg, T., Heusinkveld, B., Kabat, P.,  
653 Scott, S., Soegaard, H., and Verhoef, A.: A system to measure surface fluxes of momentum, sensible  
654 heat, water vapour and carbon dioxide, *J. Hydrol.*, 188-189, 589-611, 10.1016/s0022-1694(96)03194-  
655 0, 1997.

656 Moncrieff, J. B., R. Clement, J. Finnigan, and Meyers, T.: Averaging, detrending and filtering of eddy  
657 covariance time series, in: *Handbook of Micrometeorology: A Guide for Surface Flux Measurements*,  
658 edited by: Lee, X., W. J., Massman and B. E. Law., Kluwer Academic, Dordrecht, 7-31, 2004.

659 Mutanga, O., and Skidmore, A. K.: Narrow band vegetation indices overcome the saturation problem in  
660 biomass estimation, *Int. J. Remote Sens.*, 25, 3999-4014, 10.1080/01431160310001654923, 2004.

661 Myneni, R. B., and Williams, D. L.: On the relationship between FAPAR and NDVI, *Remote Sens.*  
662 *Environ.*, 49, 200-211, 1994.

663 Pisek, J., Ryu, Y., Sprintsin, M., He, L., Oliphant, A. J., Korhonen, L., Kuusk, J., Kuusk, A.,  
664 Bergstrom, R., Verrelst, J., and Alikas, K.: Retrieving vegetation clumping index from Multi-angle  
665 Imaging SpectroRadiometer (MISR) data at 275 m resolution, *Remote Sens. Environ.*, 138, 126-133,  
666 <http://dx.doi.org/10.1016/j.rse.2013.07.014>, 2013.

667 Psomas, A., Kneubühler, M., Huber, S., Itten, K., and Zimmermann, N. E.: Hyperspectral remote  
668 sensing for estimating aboveground biomass and for exploring species richness patterns of grassland  
669 habitats, *Int. J. Remote Sens.*, 32, 9007-9031, 10.1080/01431161.2010.532172, 2011.

670 Qi, J., Chehbouni, A., Huete, A. R., Kerr, Y. H., and Sorooshian, S.: A modified soil adjusted  
671 vegetation index, *Remote Sens. Environ.*, 48, 119-126, 1994.

672 Rasmussen, M. O., Göttsche, F. M., Diop, D., Mbow, C., Olesen, F. S., Fensholt, R., and Sandholt, I.:  
673 Tree survey and allometric models for tiger bush in northern Senegal and comparison with tree  
674 parameters derived from high resolution satellite data, *Int. J. Appl. Earth Obs. Geoinf.*, 13, 517-527,  
675 10.1016/j.jag.2011.01.007, 2011.

676 Richter, K., Atzberger, C., Hank, T. B., and Mauser, W.: Derivation of biophysical variables from  
677 Earth observation data: validation and statistical measures, *APPRES*, 6, 063557-063551-063557-  
678 063523, 10.1117/1.JRS.6.063557, 2012.

679 Roberto, C., Lorenzo, B., Michele, M., Micol, R., and Cinzini, P.: Optical Remote Sensing of  
680 Vegetation Water Content, in: *Hyperspectral Remote Sensing of Vegetation*, edited by: Thenkabail, P.  
681 S., Lyon, J. G., and Huete, A., CRC Press, Taylor and Francis Group, Boca Raton, FL, 227-244, 2012.

682 Rouse, J. W., Haas, R. H., Schell, J. A., Deering, D. W., and Harlan, J. C.: Monitoring the Vernal  
683 Advancement of Retrogradation of Natural Vegetation, Type III, Final Report, Greenbelt, MD, 1974.

684 Sandmeier, S., Müller, C., Hosgood, B., and Andreoli, G.: Physical Mechanisms in Hyperspectral  
685 BRDF Data of Grass and Watercress, *Remote Sens. Environ.*, 66, 222-233,  
686 [http://dx.doi.org/10.1016/S0034-4257\(98\)00060-1](http://dx.doi.org/10.1016/S0034-4257(98)00060-1), 1998.

687 Schaepman-Strub, G., Schaepman, M. E., Painter, T. H., Dangel, S., and Martonchik, J. V.: Reflectance  
688 quantities in optical remote sensing—definitions and case studies, *Remote Sens. Environ.*, 103, 27-42,  
689 <http://dx.doi.org/10.1016/j.rse.2006.03.002>, 2006.

690 Schopfer, J., Dangel, S., Kneubühler, M., and Itten, K.: The Improved Dual-view Field Goniometer  
691 System FIGOS, *Sensors*, 8, 5120-5140, 2008.

692 Sims, D. A., and Gamon, J. A.: Estimation of vegetation water content and photosynthetic tissue area  
693 from spectral reflectance: a comparison of indices based on liquid water and chlorophyll absorption  
694 features, *Remote Sens. Environ.*, 84, 526-537, 2003.

695 Sjöström, M., Ardö, J., Eklundh, L., El-Tahir, B. A., El-Khidir, H. A. M., Hellström, M., Pilesjö, P.,  
696 and Seaquist, J.: Evaluation of satellite based indices for gross primary production estimates in a sparse  
697 savanna in the Sudan, *Biogeosciences*, 6, 129-138, 2009.

698 Soudani, K., Hmimina, G., Dufrière, E., Berveiller, D., Delpierre, N., Ourcival, J.-M., Rambal, S., and  
699 Joffre, R.: Relationships between photochemical reflectance index and light-use efficiency in  
700 deciduous and evergreen broadleaf forests, *Remote Sens. Environ.*, 144, 73-84, 2014.

701 Tagesson, T., Eklundh, L., and Lindroth, A.: Applicability of leaf area index products for boreal  
702 regions of Sweden, *Int. J. Remote Sens.*, 30, 5619-5632, 2009.

703 Tagesson, T., Mastepanov, M., Tamstorf, M. P., Eklundh, L., Schubert, P., Ekberg, A., Sigsgaard, C.,  
704 Christensen, T. R., and Ström, L.: High-resolution satellite data reveal an increase in peak growing  
705 season gross primary production in a high-Arctic wet tundra ecosystem 1992-2008, *Int. J. Appl. Earth  
706 Obs. Geoinf.*, 18, 407-416, 2012.

707 Tagesson, T., Fensholt, R., Copley, F., Guiro, I., Horion, S., Ehammer, A., and Ardö, J.: Dynamics in  
708 carbon exchange fluxes for a grazed semi-arid savanna ecosystem in West Africa, *Agr. Ecosyst.  
709 Environ.*, 205, 15-24, <http://dx.doi.org/10.1016/j.agee.2015.02.017>, 2015a.

710 Tagesson, T., Fensholt, R., Guiro, I., Rasmussen, M. O., Huber, S., Mbow, C., Garcia, M., Horion, S.,  
711 Sandholt, I., Rasmussen, B. H., Götsche, F. M., Ridler, M.-E., Olén, N., Olsen, J. L., Ehammer, A.,  
712 Madsen, M., Olesen, F. S., and Ardö, J.: Ecosystem properties of semi-arid savanna grassland in West  
713 Africa and its relationship to environmental variability, *Global Change Biol.*, 21, 250-264, doi:  
714 10.1111/gcb.12734, 2015b.

715 Thenkabail, P. S., Smith, R. B., and De Pauw, E.: Hyperspectral Vegetation Indices and Their  
716 Relationships with Agricultural Crop Characteristics, *Remote Sens. Environ.*, 71, 158-182,  
717 [http://dx.doi.org/10.1016/S0034-4257\(99\)00067-X](http://dx.doi.org/10.1016/S0034-4257(99)00067-X), 2000.

718 Thenkabail, P. S., Enclona, E. A., Ashton, M. S., and Van Der Meer, B.: Accuracy assessments of  
719 hyperspectral waveband performance for vegetation analysis applications, *Remote Sens. Environ.*, 91,  
720 354-376, 2004.

721 Thenkabail, P. S., Lyon, J. G., and Huete, A.: Advances in hyperspectral remote sensing of vegetation  
722 and agricultural croplands, in: *Hyperspectral Remote Sensing of Vegetation*, edited by: Thenkabail, P.  
723 S., Lyon, J. G., and Huete, A., CRC Press, Taylor and Francis Group, Boca Raton, FL, 3-35, 2012.

724 Tucker, C. J.: Red and photographic infrared linear combinations for monitoring vegetation, *Remote  
725 Sens. Environ.*, 8, 127-150, [http://dx.doi.org/10.1016/0034-4257\(79\)90013-0](http://dx.doi.org/10.1016/0034-4257(79)90013-0), 1979.

726 van Leeuwen, W. J. D., Huete, A. R., and Laing, T. W.: MODIS Vegetation Index Compositing  
727 Approach: A Prototype with AVHRR Data, *Remote Sens. Environ.*, 69, 264-280,  
728 [http://dx.doi.org/10.1016/S0034-4257\(99\)00022-X](http://dx.doi.org/10.1016/S0034-4257(99)00022-X), 1999.

729 Verhoef, W., and Bach, H.: Coupled soil-leaf-canopy and atmosphere radiative transfer modeling to  
730 simulate hyperspectral multi-angular surface reflectance and TOA radiance data, *Remote Sens.*  
731 *Environ.*, 109, 166-182, <http://dx.doi.org/10.1016/j.rse.2006.12.013>, 2007.

732 Vickers, D., and Mahrt, L.: Quality control and flux sampling problems for tower and aircraft data, *J.*  
733 *Atmos. Ocean. Tech.*, 14, 152-526, 1997.

734 Webb, E. K., Pearman, G. I., and Leuning, R.: Correction of the flux measurements for density effects  
735 due to heat and water vapour transfer, *Q. J. Roy. Meteor. Soc.*, 106, 85-100, 1980.

736 Wilczak, J. M., Oncley, S. P., and Stage, S. A.: Sonic anemometer tilt correction algorithms, *Bound.-*  
737 *Lay. Meteorol.*, 99, 127-150, 2001.

738

739

740 **Tables**

741 Table 1. Information about the sensor set-up for the measured environmental variables. HCRF is hemispherical conical reflectance  
 742 factor; GPP is gross primary productivity; LUE is light use efficiency; and FAPAR is fraction of photosynthetically active radiation  
 743 absorbed by the vegetation. Min and Max are minimum and maximum values measured, respectively; DW is dry weight; C is carbon;  
 744 and MJ is megajoule.

Variable	Unit	Sensors	Sensor company	Data size	Aggregation method	Data gaps	Min	Max
Hyperspectral HCRF	-	Fieldspec 3	ASD Inc., Colorado, USA	371	Daily median	31%	0	1
Herbaceous biomass	g DW m <sup>-2</sup>	-	-	12	Daily mean 28 plots	-	0	223
GPP	g C d <sup>-1</sup>	LI-7500, GILL R3	LI-COR Inc., Lincoln, USA; Gill instruments, Hampshire, UK	285	Daily sums	56%	-14.22	-0.22
LUE	g C MJ <sup>-1</sup>	LI-7500, GILL R3	LI-COR Inc., Lincoln, USA; Gill instruments, Hampshire, UK	272	Daily estimates	28%	0.02	1.89
FAPAR	-	Quantum SKP 215	Skye instruments Ltd., Llandridod wells, UK	369	Daily averages 10:00-16:00	1%	0.07	0.77

745  
746

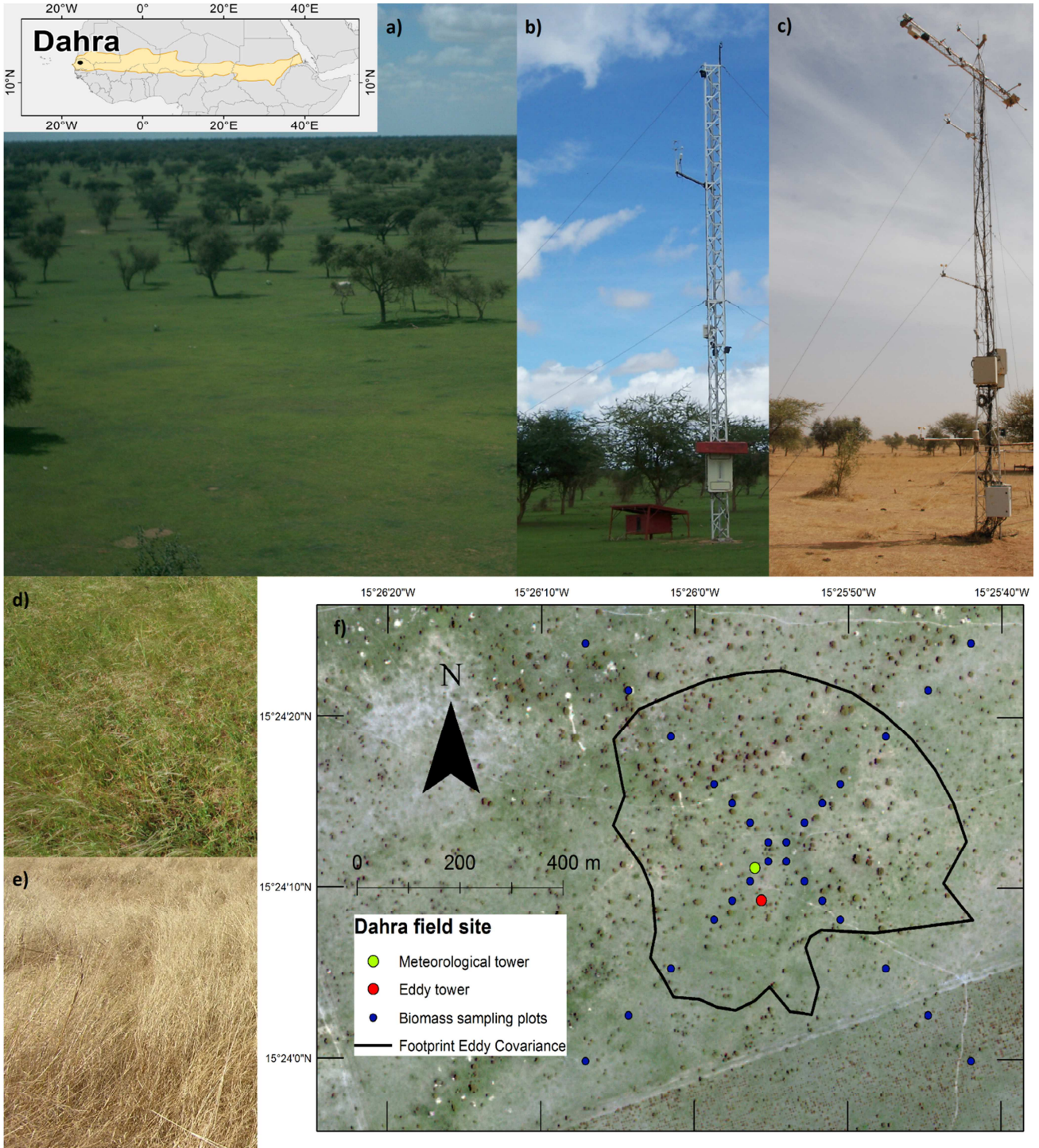
747 Table 2. Wavelengths of the hemispherical conical reflectance factors (HCRF) ( $\rho_{i,j}$ ) used in the  
 748 normalized difference spectral indices (NDSI) that generated the strongest correlations with ecosystem  
 749 properties. DW is dry weight; FAPAR is the fraction of photosynthetically active radiation absorbed by  
 750 the vegetation; AVG is average; SD is standard deviation; RMSE is root-mean-square-error.

Ecosystem property	Sample size	$\rho_i$	$\rho_j$	$R^2$	Observation (AVG $\pm$ SD)	RMSE
Biomass (g DW m <sup>-2</sup> )	12	587	705	0.88 $\pm$ 0.07	153 $\pm$ 59	28.4 $\pm$ 8.7
Gross primary productivity (g C m <sup>-2</sup> d <sup>-1</sup> )	285	518	556	0.86 $\pm$ 0.02	-4.3 $\pm$ 4.0	1.5 $\pm$ 0.1
Light use efficiency (g C MJ <sup>-1</sup> )	272	688	436	0.81 $\pm$ 0.02	0.53 $\pm$ 0.65	0.26 $\pm$ 0.02
FAPAR	369	399	1295	0.81 $\pm$ 0.02	0.41 $\pm$ 0.16	0.06 $\pm$ 0.003

751  
752

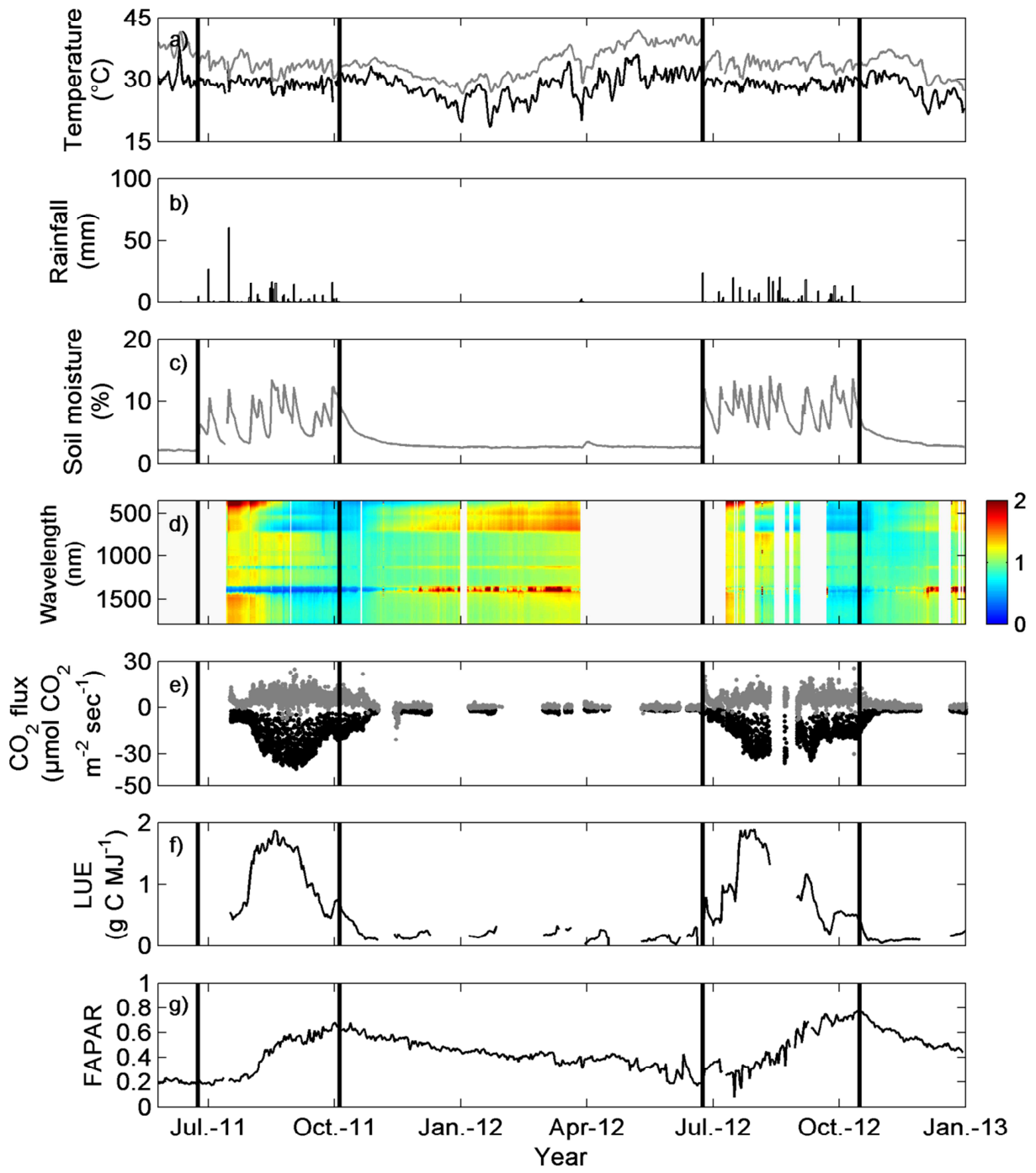


753 **Figures**



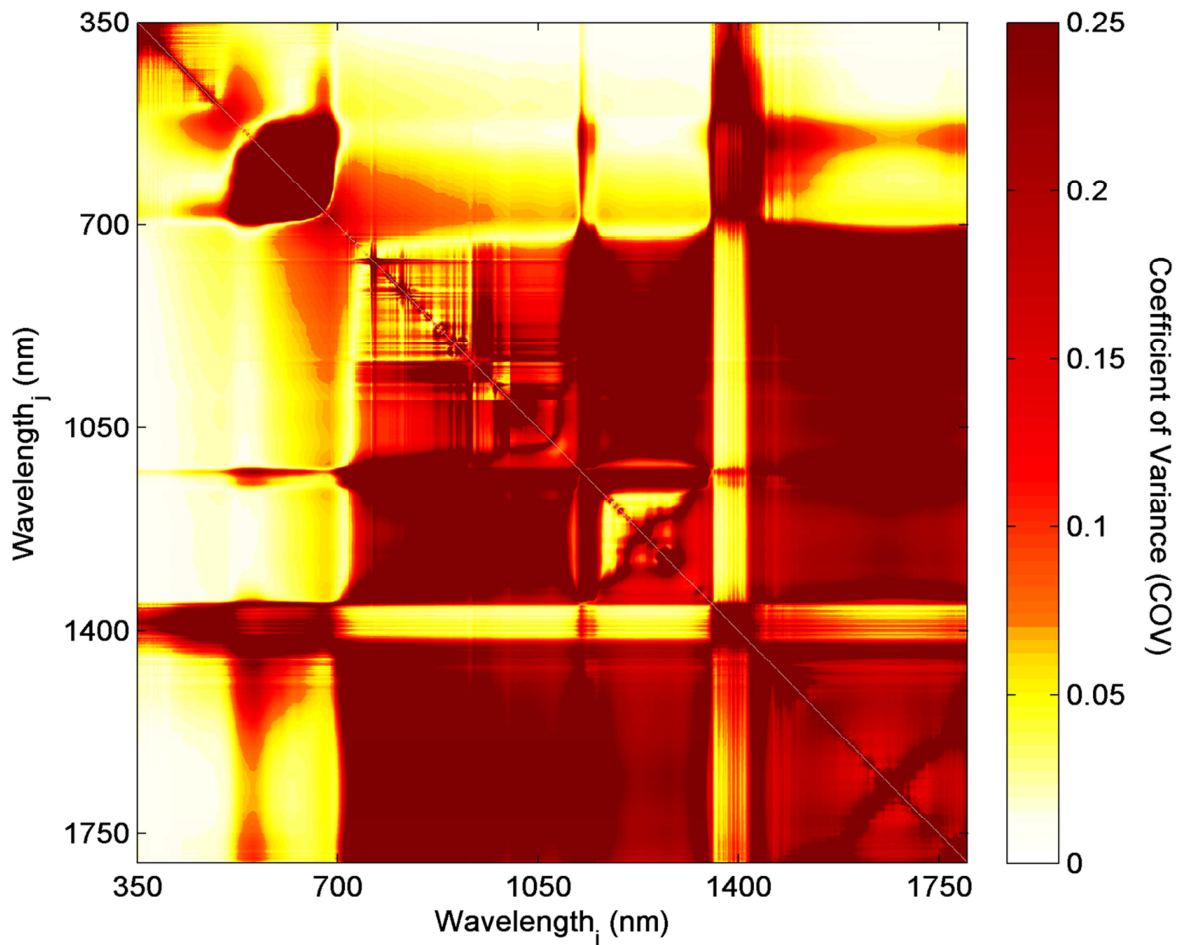
754  
755 Figure 1. Map and photos of the Dahra field site and measured areas. The map shows the location of  
756 Dahra within the Sahel (orange area). a) Photo of the footprint of the eddy covariance (EC) tower; b)

757 photo of the EC tower; c) photo of the meteorological tower with the spectroradiometers; d) photo of  
758 the instantaneous field of view (IFOV) of the spectroradiometers during the rainy season; e) photo of  
759 the IFOV of the spectroradiometer during the beginning of the dry season; and f) Quickbird image from  
760 the Dahra field site from 11 September 2011 showing the location of the meteorological tower, the EC  
761 tower, the biomass sampling plots and the footprint of the EC measurements. The EC footprint area is  
762 the median 70% cumulative flux distance from the eddy covariance tower. The photos of the EC  
763 tower and its footprint are taken during the rainy season whereas the photo of the meteorological tower  
764 shows the late dry season.  
765

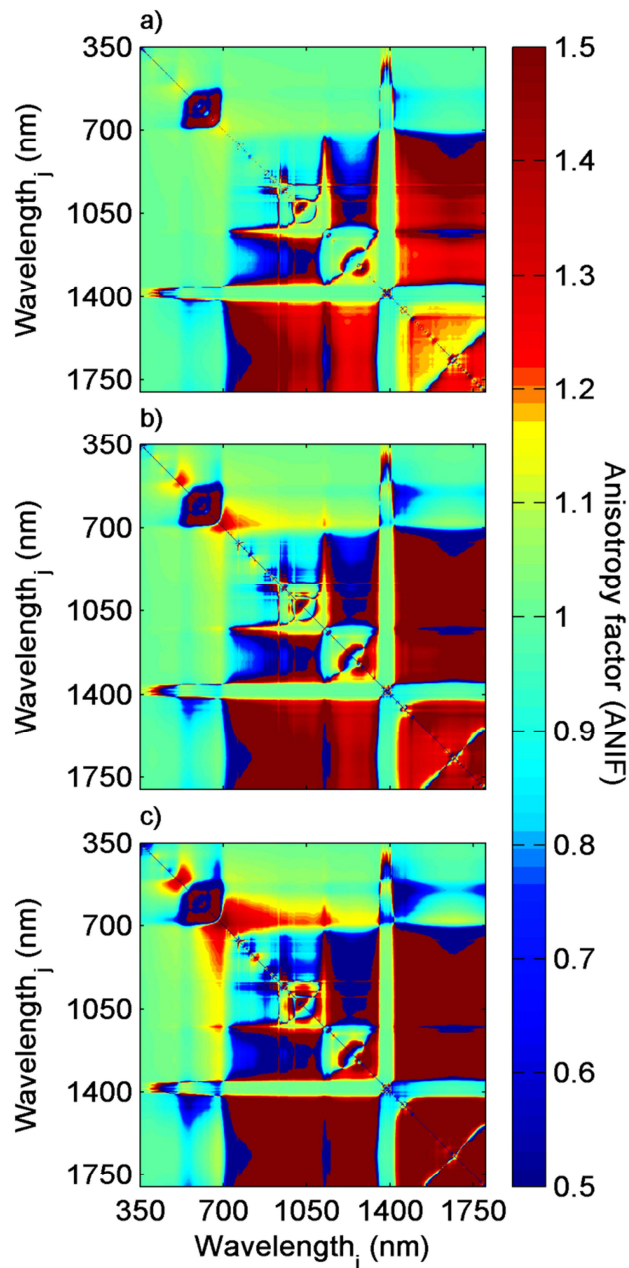


766  
 767 Figure 2. Time series of the measured variables: a) daily averaged air temperature (black line), and soil  
 768 temperature at 0.05 m depth (grey line), b) daily sums of rainfall, c) daily average of soil moisture at  
 769 0.05 m depth, d) hyperspectral hemispherical conical reflectance factor (HCRF) normalized by

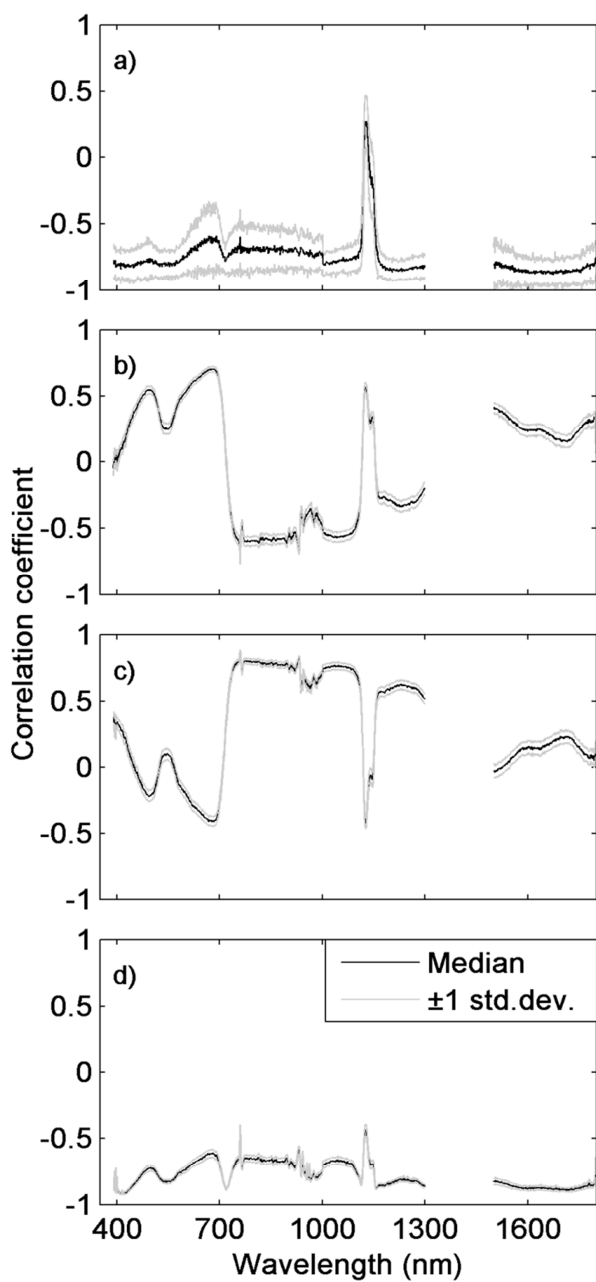
770 calculating the ratio between daily median HCRF for each wavelength (350-1800 nm) and the average  
771 HCRF for the entire measurement period, e) gross primary productivity (GPP) (black dots) and  
772 ecosystem respiration (grey dots), f) the light use efficiency (LUE), and g) the fraction of  
773 photosynthetically active radiation absorbed by the vegetation (FAPAR). The black vertical lines are  
774 the start and end of the rainy seasons (first and final day of rainfall). The gaps are caused by technical  
775 issues due to loss of power supply, broken sensors or filtering of data due to bad weather conditions.  
776



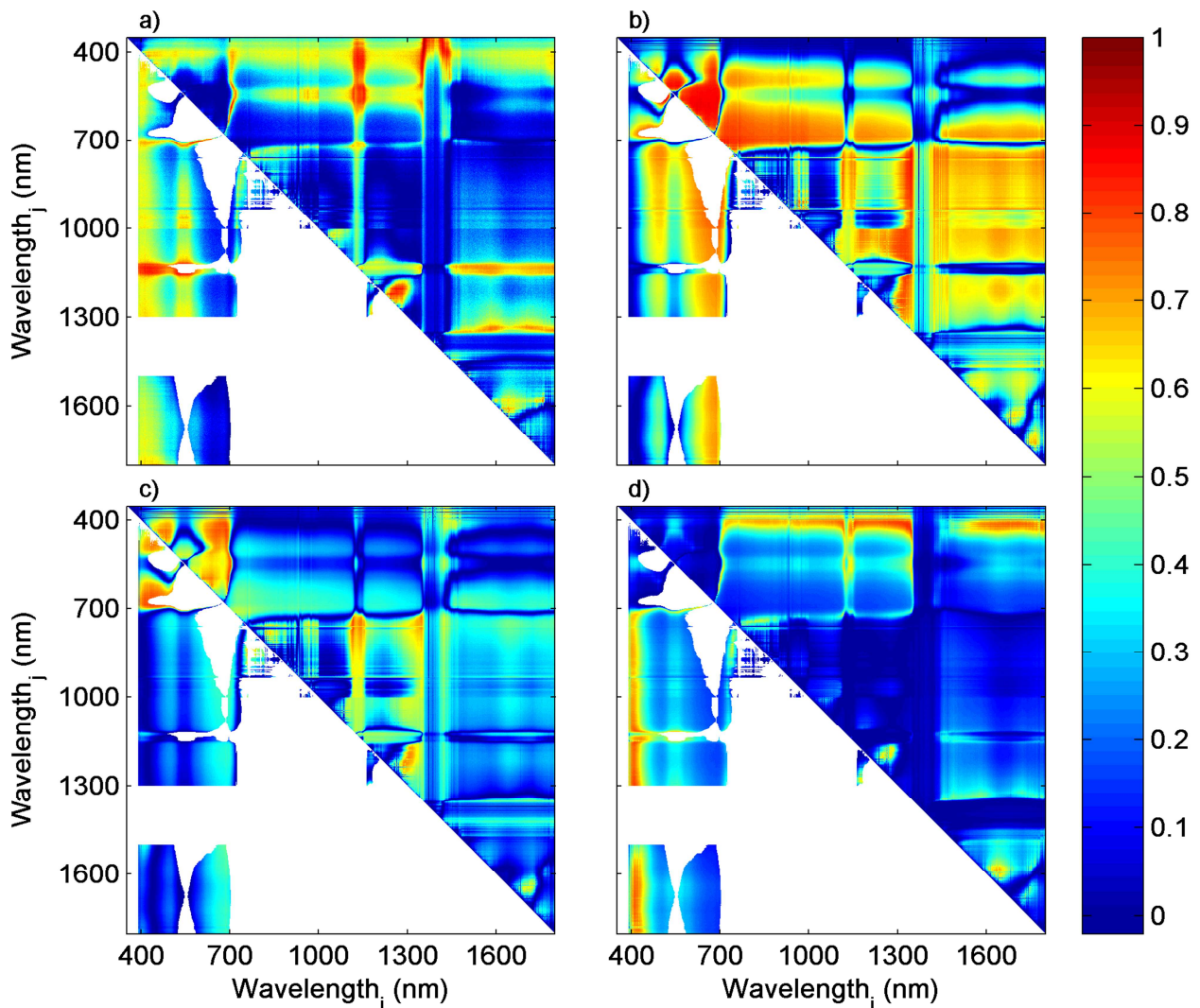
777  
 778 Figure 3. The coefficient of variation (COV), i.e. the ratio between daily standard deviation and the  
 779 daily mean (measurements taken between 8:00 and 18:00), for different normalised difference spectral  
 780 index (NDSI) wavelength ( $i, j$ ) combinations for 12 days at the peak of the growing season 2011 (day of  
 781 year 237-251;  $n=576$ ). The COV indicates how strongly the NDSI are affected by variable sun angles.  
 782



783  
 784 Figure 4. The anisotropy factor (ANIF) for different normalised difference spectral index (NDSI)  
 785 wavelength ( $i, j$ ) combinations for 15 days at the peak of the growing season 2011 (day of year 237-251)  
 786 for the different sensor viewing angles: a) 15°, b) 30°, and c) 45°. The sensor is pointing east and west  
 787 in the lower left and upper right corners of each plot, respectively. In order not to include effects of  
 788 solar zenith angles in the analysis, only data measured between 12:00 and 14:00 were used in the ANIF  
 789 calculations (n=48).  
 790  
 791

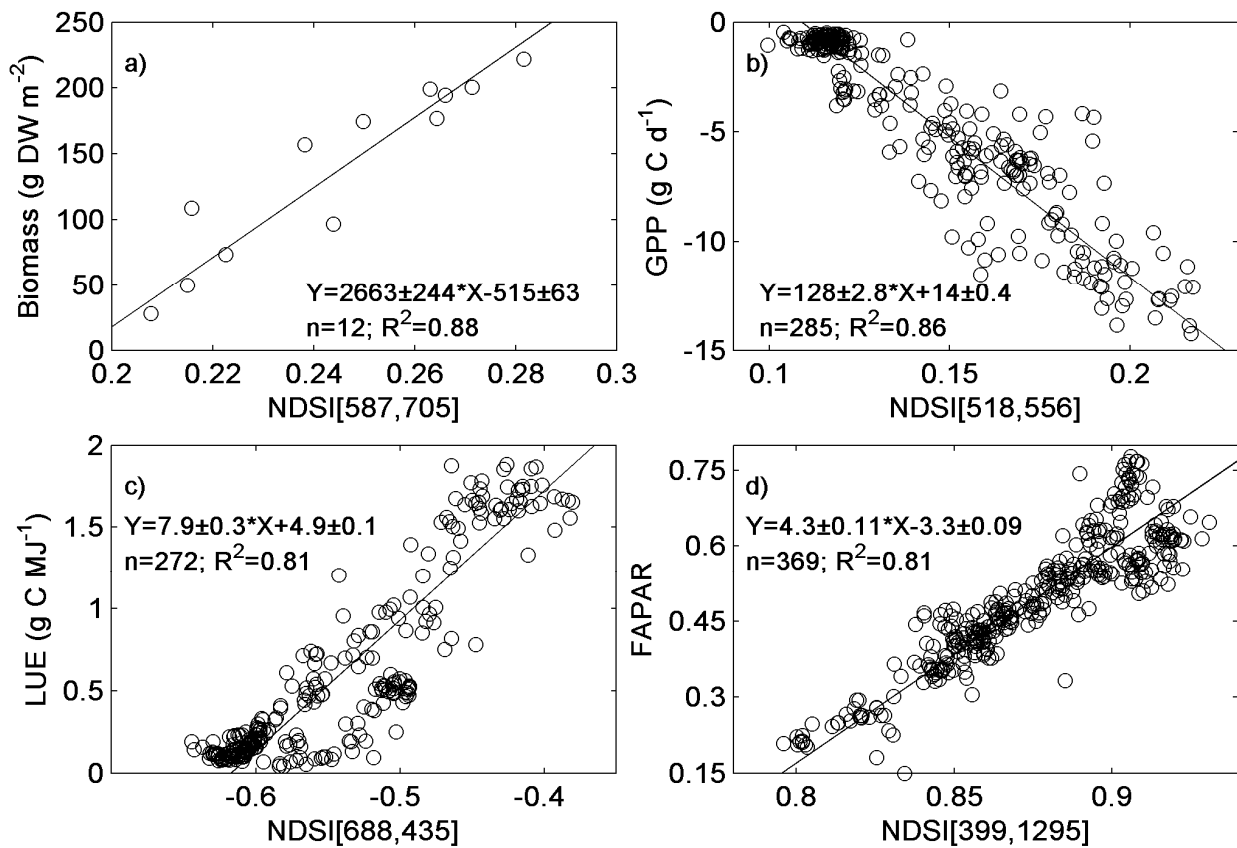


792  
 793 Figure 5. Median correlation coefficient ( $\pm 1$  standard deviation) between seasonal dynamics in  
 794 hyperspectral hemispherical conical reflectance factors (HCRF) 2011-2012 and a) dry weight biomass  
 795 ( $n=12$ ;  $\text{g m}^{-2}$ ), b) gross primary productivity (GPP) ( $n=285$ ;  $\text{g C day}^{-1}$ ), c) light use efficiency (LUE)  
 796 ( $n=272$ ;  $\text{g C MJ}^{-1}$ ), and d) fraction of photosynthetically active radiation absorbed by the vegetation  
 797 (FAPAR) ( $n=369$ ).  
 798  
 799



800  
 801 Figure 6. Coefficient of determination ( $R^2$ ) between normalised difference spectral index (NDSI) and a)  
 802 dry weight biomass ( $n=12$ ;  $\text{g m}^{-2}$ ), b) gross primary productivity (GPP) ( $n=285$ ;  $\text{g C day}^{-1}$ ), c) light use  
 803 efficiency (LUE) ( $n=272$ ;  $\text{g C MJ}^{-1}$ ), and d) fraction of photosynthetically active radiation absorbed by  
 804 the vegetation (FAPAR) ( $n=369$ ). The upper right half of each image shows the unfiltered  $R^2$  values,  
 805 whereas the lower left half shows filtered  $R^2$ , based on the filtering criteria described under Subsect.  
 806 2.6.  
 807





808

809

810

811

812

Figure 7. The least square linear regressions with the strongest relationships between the normalised difference spectral index (NDSI) and a) dry weight biomass, b) gross primary productivity (GPP), c) light use efficiency (LUE), and d) fraction of photosynthetically active radiation absorbed by the vegetation (FAPAR). In the equations, the slope and intercepts ( $\pm 1$  standard deviation) is given.